

ARTICLE

Interfacial Analysis of PEM Electrolyzer Using X-ray Computed Tomography

Emily Leonard^a, Andrew D. Shum^b, Nemanja Danilovic^c, Christopher Capuano^d, Katherine E. Ayers^d, Lalit M. Pant^c, Adam Z. Weber^c, Xianghui Xiao^{e,f}, Dilworth Y. Parkinson^g, Iryna V. Zenyuk^{a,b,h,*}

Received 00th January 20xx,
Accepted 00th January 20xx

DOI: 10.1039/x0xx00000x

Polymer electrolyte membrane (PEM) electrolyzers are electrochemical energy-conversion devices that convert electricity into hydrogen fuel at high efficiencies. The interface between the porous transport layer (PTL) and catalyst layer is of interest from a transport perspective, as this interface is rough, reducing contact between the layers. Electrons, protons, water and oxygen have to simultaneously meet at this interface and there is a need to understand the optimal morphology. In this study we use operando X-ray computed tomography (CT) and X-ray radiography to visualize operation of PEM electrolyzers under two current densities: 500 and 800 mA/cm². First, we compare performance of catalyst-coated membranes (CCM) electrolyzers with porous transport electrode (PTE) electrolyzers by correlating polarization curves to interface morphology observed with X-ray CT. At 1 A/cm², the micro-CT CCM electrolyzer showed 200 mV improvement in potential primarily due to better contact between the electrocatalyst, membrane, and PTL. From the nano-CT imaging we discovered non-homogeneous distribution of IrO_x electrocatalyst. The modeling study shows that the primary reason for performance loss in PTE configuration is due to low connectivity of catalyst particles with membrane. This causes bottlenecks in proton transport and results in high ionic potential losses in the anode. Then, we compared the polarization behavior and morphology of cells with CCMs but two types of PTLs. One was made with sintered titanium and the other with titanium fiber. The Ti fiber PTL showed higher porosity and lower tortuosities, however these better morphological properties did not necessarily translate into significantly lower potentials (45 mV difference), as the electrolyzer was not operated above 1 A/cm². This was also confirmed by radiography study, where oxygen residence time in the channels showed similar fractions for both types of the PTLs.

Introduction

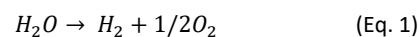
Renewable energy sources are desirable for electricity generation due to no emission of greenhouse gases (GHGs)². Electricity is mainly produced from the combustion of fossil fuels (e.g. coal, oil, natural gas) which have a significant amount of GHG carbon dioxide (CO₂)³. The electric grid is generally designed to provide electricity to meet instantaneous demand. Natural fluctuation and intermittency of renewable resources pose challenges to implementing renewable-based energy sources without coupling them to energy storage media.^{4,5,6}

Energy carriers (e.g. natural gas, liquid hydrocarbon fuels, hydrogen gas) allow the transport and delivery of energy to an end user^{5,7}. Hydrogen is a very suitable option to be a primary energy

carrier because of its high energy density. Water electrolysis can be used to produce hydrogen with renewable electricity, where electricity is used to electrochemically split water molecules⁸. Hydrogen can then be stored in compressed form, liquid form or transported via natural gas pipelines. Hydrogen can potentially mitigate grid intermittency challenges. The European framework to use hydrogen as a fuel carrier is known as Power-to-Gas^{4,5}, and it is a critical aspect of the Department of Energy (DOE's) plan, H2@Scale⁹.

Alkaline (KOH-based) and proton exchange membrane (PEM) electrolyzers are the two main systems on the market today. In alkaline electrolysis systems, the cell anode and cathode are separated by a diaphragm and submerged in a liquid electrolyte¹⁰. The limited pressure differential across the cell due to the liquid electrolyte is a major limitation of the technology⁵. PEM electrolyzers, on the other hand, use a membrane as both an electrolyte and physical barrier to separate the product gases. PEM electrolyzers require expensive materials, but are more responsive to changes in voltage, can be operated at higher pressures (balanced and differential), and typically generate a purer product at the system outlet than alkaline water electrolyzers¹¹.

The overall water electrolysis reaction is expressed as:



Eqn. 1 can be further broken down into two half-cell reactions. On the anode, the oxygen evolution reaction (OER) describes the oxidation of water. On the cathode, the hydrogen evolution reaction

^a Department of Chemical and Biological Engineering, Tufts University, Medford, MA, USA

^b Department of Mechanical Engineering, Tufts University, Medford, MA, USA

^c Lawrence Berkeley National Laboratory, Berkeley, CA, USA

^d Nel Hydrogen, Wallingford, CT, USA

^e X-ray Science Division, Argonne National Laboratory, 9700 S. Class Avenue, Lemont IL, USA

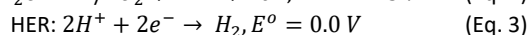
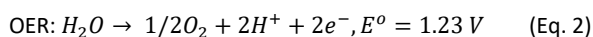
^f National Synchrotron Light Source, Upton, NY, USA

^g Department of Chemical and Biomolecular Engineering; National Fuel Cell Research Center, University of California, Irvine, CA, USA

* Corresponding author: Iryna.Zenyuk@uci.edu

Electronic Supplementary Information (ESI) available: [Additional morphological information, electrochemical data, and modelling parameters are shown in the Supplementary Information]. See DOI: 10.1039/x0xx00000x

(HER) describes the reduction of hydrogen gas:



Standard potentials listed in **Eqns. 1 and 2** are with respect to the standard hydrogen electrode (SHE). Overpotentials can be attributed to inefficiencies such as kinetic, ohmic, and mass transfer losses. Typically, at low current densities, kinetic losses are dominant and they maintain influence as current density increases. For an electrolyzer, kinetic losses are mostly attributed to the charge transfer in the OER reaction on the anode, which is the limiting half-cell reaction. Ohmic losses scale linearly with current density, and finally mass transfer losses largely contribute to the overpotentials at higher current densities, above $\sim 1.5 \text{ A/cm}^2$ ¹². Due to the OER kinetics and ohmic resistances having sustained influence on electrolyzer overpotentials, these two characteristics have been studied in an effort to increase PEM electrolyzer efficiencies¹³.

The structure of the membrane electrode assembly (MEA) of a PEM electrolyzer is comparable to a proton exchange membrane (PEM) fuel cell. When focusing on materials, however, the two differ on the anode transport layer (cathode for fuel cells). Fuel cells typically implement carbon paper for both anode and cathode transport layers known as gas diffusion layers (GDLs). The anode side of an electrolyzer operates at potentials over 1.23 V and therefore fosters an environment too corrosive for a carbon-based transport layer. For this reason, a porous titanium metal layer is used as the porous transport layer (PTL) resists corrosion¹⁴⁻¹⁶. There are multiple processing techniques that allow porosity and tortuosity to be tuned facilitating the transport of water, gas and electrons through the network¹¹.

In fuel cells, catalyst ink consists of electrocatalyst, ionomer and a conductive support (usually carbon based^{17, 18}). Again, corrosive potentials on the electrolyzer anode limit material options. Currently, the electrolyzer anode catalyst layers consist of ionomer and electrocatalyst, with high electrocatalyst loadings (around 2-3 mg/cm² for iridium oxide (IrO_x) electrocatalyst^{13, 19, 20}) to compensate for the lack of conductive support. In-plane conductivity and uniform catalyst distribution are two catalyst layer properties that may suffer in the absence of a support.

Adding a micro-porous layer (MPL) to the GDL is a technique that has been studied and implemented in the fuel cell community to improve contact between the GDL and catalyst layers. Without MPLs in electrolyzers, there is limited contact between the PTL and catalyst layer which presents a transport challenge. To improve contact in electrolyzers, there have been efforts to create a porosity gradient across the thickness of the PTL^{15, 21}. Furthermore, oxygen nucleation, growth and transport through the PTL is currently not well-explored⁶.

Several imaging techniques have been used so far to connect morphology of the porous layers to water and oxygen transport. Seweryn, et. al. used neutron imaging to investigate content of oxygen during PEM electrolyzer operation. Their work demonstrated a surprising dynamic equilibrium between the two phases that was relatively constant across a wide range of current densities, the lowest of which was 0.1 A/cm². This would suggest that the PTL (in this case, sintered titanium) was saturated with oxygen close to the

membrane interface even at low current densities¹⁶. X-ray computed tomography (X-ray CT) has been used as an *ex-situ* technique to characterize the morphology of electrolyzer PTLs^{12, 22}. In our previous work we were the first ones to use X-ray CT and X-ray radiography to investigate the oxygen bubble formation and removal in an operating PEM electrolyzer²³. We observed oxygen bubbles at low current densities transitioning into oxygen slugs (gas occupying the entire channel) at high current densities. Bubble residence, which was defined as the time the bubble spent in the channel before being detached, decreased with increase in current density. This is because oxygen is generated and detached faster at higher current densities. Another major finding was mechanical removal of electrocatalyst at the interface with the PTL, which worsened at higher current densities. The mechanical removal of the electrocatalyst was due to oxygen bubbles exchanging momentum with electrocatalyst and inducing mechanical stress.

In this study we focus on the interfacial contact between the transport layers and the catalyst particles in an electrolyzer cell using X-ray CT. We compare porous transport electrode (PTE) and catalyst coated membrane (CCM) MEA configurations as well as two different PTL titanium morphologies. The PTE is selected as an alternative to a CCM, as the PTE fabrication method allows flexibility in membrane selection, higher conformity of catalyst to the PTL and potentially longer shelf life of the electrode. Using X-ray radiography, a transient technique, we observe oxygen content in the channel during operation at 50°C and under two applied current densities. Furthermore, using nano X-ray CT imaging we visualize the electrocatalyst distribution within the CCM. Using continuum modeling we sought to further understand the performance of the two electrolyzer MEA configurations.

Experimental

X-ray Computed Tomography (CT) experiments

Electrolyzer tomographic and radiographic images were acquired at Argonne National Laboratory (ANL), Lawrence Berkeley National Laboratory (LBNL) and Brookhaven National Laboratory (BNL). At ANL, image acquisition was performed on beamline 2-BM-A at the Advanced Photon Source (APS) using a 20 μm LuAG scintillator, 5x lenses, and a sCMOS PCO Edge camera. Images have a 1.3 μm voxel resolution and a horizontal field of view (FOV) of 3.3 mm. A double-multilayer monochromator was used to select a beam energy of 40 keV.

At LBNL, image acquisition was performed at Beamline 8.3.2 at the Advanced Light Source (ALS) using a 50 μm LuAg:Ce scintillator, 5x lenses, and a sCMOS PCO Edge camera. Images resulted in a voxel resolution of 1.3 μm and a horizontal field of view (FOV) of 3.3 mm. A double multilayer monochromator was used to select a beam energy of 30 keV.

Tomography scans require a sample rotation of 180° to collect the projections for a three-dimensional reconstruction. One FOV was collected per condition and each scan did not exceed 30 minutes of continuous X-ray exposure (during both tomography and radiography). X-ray radiography does not require sample rotation. Radiographic projections were collected with an exposure time of 50

ms in both thru-plane and in-plane orientations. For this experiment, thru-plane is defined as perpendicular to the MEA layers and in-plane is defined as parallel to the MEA layers.

Nano X-ray CT was collected at beamline 18-ID Full Field X-ray Imaging (FXI) at National Synchrotron Light Source II (NSLS II) at BNL. Imaging was performed at 8 keV selected energy, 30 nm spatial resolution with 40 μm FOV. The scan-time was less than one minute in absorption-contrast mode.

Materials

Three distinct water electrolyzer cells were assembled for the micro X-ray CT and radiography experiments. The PTE system had sintered titanium (provided by Nel, Wallingford, CT) and Toray TGP-H-120 carbon paper for the anode and cathode, respectively. The anode catalyst was iridium-based (IrO_x) with a loading of 3 mg/cm^2 and the cathode had a platinum-based catalyst loading of 2 mg/cm^2 . Nafion ionomer solution (1100 EW, 5 wt% ionomer; D521 from Ion Power, USA) was used for cathode and anode inks. The PTE was prepared by a proprietary procedure in which it is etched and coated with a small amount of Pt for improved contact resistance. Ir was then deposited from a Nafion based ink using an ultrasonic spray coater. Nafion-117 (purchased from Fuel Cell Store, College Station, TX) was used for the PEM. These three layers made up the PTE MEA. The MEA for the two CCM electrolyzers consisted of a PTL on the anode, a CCM, and a GDL on the cathode. The CCMs had the same iridium-based (IrO_x) anode catalyst with a loading of 2.2 mg/cm^2 and a platinum-based cathode catalyst loading of 1.0 mg/cm^2 . Each system had the same CCM (both received from Nel, Wallingford, CT) and GDL (carbon paper). The only component that changed was the PTL morphology and we compared sintered titanium to titanium fiber (Nel, Wallingford, CT).

Hardware Design

Due to its properties of X-ray transparency and electric conductivity, graphite was chosen for the bipolar plates (BPP). Fuel cell grade graphite (Fuel Cell Store, College Station, TX) was machined using a micro-mill. Graphite corrodes under high applied potentials of the anode, however the corrosion currents are on the order of $\sim 1 \text{ mA}/\text{cm}^2$ or less²⁴. The electrolyzers were not operated longer than eight hours per beamtime and upon visual inspection the surface of the bipolar plates remained smooth after the experiments indicating no observable degradation during this short test. Aluminum clamps and bolts were used to compress the MEA and gaskets between the graphite plates completing the micro-CT operando cell shown in **Figure 1**.

The X-ray transparent portion of the micro-CT cell is 2 cm in length and has two parallel channels (1 mm x 1 mm) separated by 1 mm of land. Kapton film was used to mask the CCM or PEM to achieve a 1 cm^2 active area. Slightly larger transport layers (electrodes, PTLs, and GDLs) were cut to completely cover the active area and incompressible Teflon-coated fiberglass (Fuel Cell Store, College Station, TX) was cut as gaskets for the transport layers on the anode and cathode sides. Electrochemical impedance spectroscopy (EIS) measurements were used to make sure the cell was compressed such that cell resistance was less than 3 Ω (Supplementary Material (SM), **Figure S3**). Thermocouples (positioned on top of the parallel

channels) and cartridge heaters allowed the cell to be heated, and maintained at 50°C using a proportional-integral differential (PID) controller.

Electrochemical characterization

Copper wire electric leads were coiled around the graphite plates via the extended tab (**Figure 1a**) to establish an electric connection. Water was introduced at the top inlet on the anode side using PEEK tubing with a syringe pump (Harvard Apparatus, Holliston, MA) at a flow-rate ranging from 0.8 mL/min to 1.6 mL/min depending on the sample and chronopotentiometric conditions. Electrochemical chronopotentiometric holds were conducted with Gamry1000E potentiostat/galvanostat (Gamry Instruments, Warminster, PA). The portable size of the potentiostat/galvanostat allows for the transportation to the synchrotron source. The current limit is 1 A for Gamry1000E limiting this study to 1 A or below. Steady-state performance was achieved by operating the cell for 5 minutes at each condition prior to X-ray CT scanning.

Once the micro-CT cell sample was loaded onto the beamline stage (**Figure 1b**), we introduced water to the system. A tomography scan was taken at open circuit voltage (OCV) as a reference image to observe the sample's morphological properties. After the tomography scan, radiography was conducted for 30 seconds in the in-plane and thru-plane orientations at OCV. These scans depicted the cell in a fully flooded condition which would be used to normalize the radiography scans at the two operating conditions.

Radiography scans consisted of two current density conditions, 500 mA/cm^2 and 800 mA/cm^2 . Current densities were chosen to ensure that the active area of each sample was tested under the

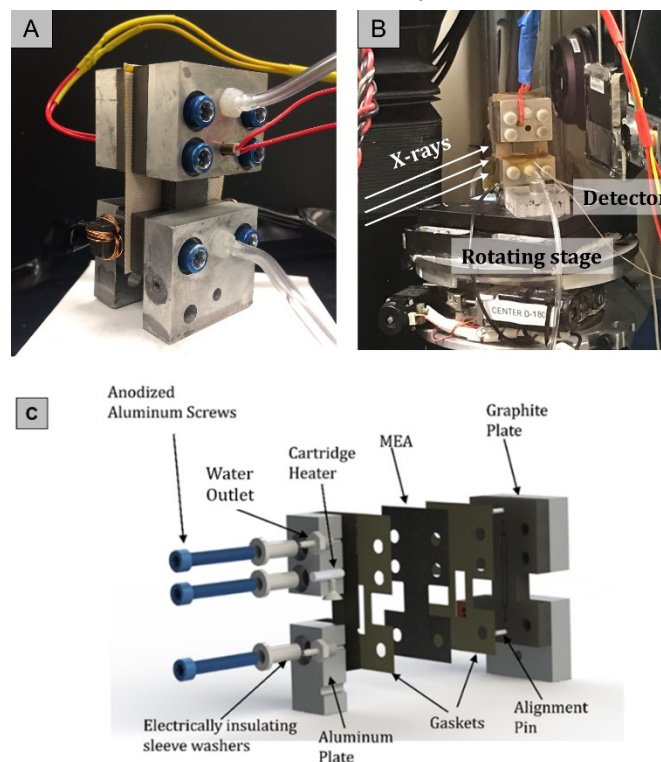


Figure 1. The micro-CT operando cell (a) pictured standalone, compressing an MEA, with a view of the 2 cm X-ray transparent window, (b) pictured installed on the ALS beamline stage, and (c) as a labeled volume rendered schematic, depicting the parallel channels milled into the graphite plate BPPs.

same operating condition. Thru-plane and in-plane radiographs were collected at a temporal resolution of 50 ms over a total scan time of 30 seconds. An EIS test and polarization curves were taken after the OCV, 500 mA/cm² and 800 mA/cm² scans. A frequency range from 500 kHz to 100 mHz was used with a 5 mV AC perturbation for the EIS experiments. Polarization curves were recorded from 1.3 V until the potential that corresponded to 1 A/cm² of current density. The scan rate was 5 mV/s and the sweep was conducted in the direction of increasing potential. Five polarization curves were collected prior X-ray CT imaging and post X-ray CT imaging for each cell.

Image processing and visualization

Two-dimensional images are acquired while the sample rotates 180° in the path of the X-ray beam. A tomographic reconstruction combines these images into a three-dimensional rendering. Tomographic reconstructions and phase retrieval were performed using the Gridrec algorithm²⁵⁻²⁷ with TomoPy²⁸. In our previous publications we describe the reconstruction process in detail^{29,30}. Image processing, 8-bit conversion, transformations and analysis were carried out with Fiji/ImageJ³¹. Segmentation of the image was performed manually for the solid (titanium or carbon paper) and voids of the transport layers and to isolate the catalyst particles. Segmented PTL layers were analyzed for porosity and tortuosity using the MatLab application TauFactor¹. Pore size distribution (PSD) was determined using the BoneJ macro³² available in ImageJ/Fiji. To identify the bubble formation in the radiography experiments the data was normalized to the corresponding OCV condition because at OCV no oxygen bubbles are evolving in the channels. As such, the radiographs reported in this work represent the applied current density conditions normalized to the corresponding sample OCV condition. The presence of oxygen bubbles was determined by mapping the greyscale pixel values over time across the water channels.

Interface Analysis

Using tomography data for the two electrolyzer comparisons (PTE vs. CCM and sintered titanium PTL vs. titanium fiber PTL), we were able to quantify the interfacial contact of the catalyst and bordering phases. After ensuring that all three phases (PTL, catalyst, PEM) were captured in the through-plane direction, we cropped sub-samples with a 1 mm² area parallel to the interface. An area of 1 mm² was used because the corresponding volumes based on the PTL thickness were larger than the REV determined by TauFactor (See SM, Figure S5). The sample selection allowed a minimum of three unique system interfaces per electrolyzer configuration.

Due to their density, the anode and cathode catalyst particles are the most highly X-ray attenuating materials on their respective sides of the micro-CT cell. For this reason, the catalyst is distinguishable from other features. As a conservative measure, when segmenting the catalyst particles, we remained consistent across the sample pool by assigning only the most attenuating features the value of '255' and all else '0'. This method was in good agreement with the greyscale reconstruction and minimized overlap with the non-catalyst features. For the purposes of this investigation,

minimizing the pixel redundancy while segmenting the different phases is crucial to reporting triple phase contact area (TPCA). TPCA is the interfacial area where the catalyst particles are in contact with both the PEM and the respective transport layer (PTL or GDL).

Once the phases were segmented, an interfacial projection of each phase was generated. In this application, a projection is the coverage area for the phase of interest over the thru-plane distance of ~5 μm. This thickness was chosen as a representation of the interface because the interfaces are not perfectly flat.

Projections were re-segmented and the phases of interest (i.e. catalyst particles, titanium, membrane) were set to '1' and all else '0'. Corresponding projections were multiplied to determine overlap (resulting pixel values of '1'). The equation for TPCA is described as:

$$TPCA\% = \frac{Overlap_{pix}}{Catalyst_{pix}} * 100\% \quad (\text{Eq. 4})$$

where $TPCA\%$ is the triple phase contact area, $Catalyst_{pix}$ is the quantity of pixels representing the catalyst features at the interface and $Overlap_{pix}$ is the quantity of catalyst pixels overlapping with the PTL and PEM after projection multiplication.

Modeling

A 2-D macro-homogeneous model was developed for simulating the performance of the different electrolyzer configurations. A 2-D MEA cross-section is used as the simulation domain. Figure S5 shows the modeling domains for both the CCM and PTE configurations. In CCM configuration a uniform catalyst layer is assumed to be in contact with the membrane. The roughness of the PTL is modeled using a hybrid layer approach. While the majority of the PTL is modeled as macro-homogeneous media, close to the catalyst a discrete micro-structure consisting of solid and pores is assumed. The discrete points of contact between PTL and catalyst will be able to elucidate the effects of in-plane electronic conductivity in catalyst. For the PTE configuration, the entire catalyst layer is assumed to consist of discrete catalyst particles supported on the PTL solid phase. To account for the low connectivity of these catalyst particles to membrane, small points of contact are assumed between catalyst and membrane.

The mathematical framework for modeling multi-component diffusion, gas and liquid convection, electronic conduction, heat conduction, proton transport, and membrane water transport is adapted from PEM fuel cell model presented by Zenyuk *et al.*³³. The reaction kinetics for HER and OER are given as:

$$j_{rxn,OER} = j_{OER} \left(1 - 0.023 \frac{j_{OER}}{1[A/m^2]} \right), \quad (\text{Eq. 5})$$

$$j_{OER} = i_{0,OER} \left[RH \exp \left(\frac{\alpha_{OER,aF}}{RT} \eta \right) - \frac{p_{O_2}}{p_{ref}} \exp \left(-\frac{\alpha_{OER,cF}}{RT} \eta \right) \right], \quad (\text{Eq. 6})$$

$$j_{HER} = i_{0,HER} \left[\exp \left(-\frac{\alpha_{HER,cF}}{RT} \eta \right) - \frac{p_{H_2}}{p_{ref}} \exp \left(\frac{\alpha_{HER,aF}}{RT} \eta \right) \right]. \quad (\text{Eq. 7})$$

Several of the layer properties and correlations are the same between PEM electrolyzer and fuel cell, and therefore are the same

as discussed by Zenyuk *et al.*³³. The simulation parameters unique to this analysis are given in **Table S1**.

Results and Discussion

PTE and CCM Electrolyzer Configurations

Figure 2 shows the cross sections for the PTE and CCM electrolyzer configurations. The high X-ray attenuation of the anode and cathode catalyst particles make it easy to see the differences between the two MEAs. For the PTE (**Figure 2a**) the catalyst inks are deposited directly on both transport layers. It can be seen clearly at the cathode-PEM interface that the catalyst particles follow the non-uniform topography of the carbon paper GDL. This feature is more subtle at the anode-PEM interface where anode catalyst particles follow the topography of the sintered titanium. In **Figure 2b** the CCM configuration has lower anode and cathode catalyst loading as the cross section reflects, and the catalyst was deposited on the surface of the PEM, which is morphologically uniform relative to the transport layers.

Three dimensional renderings of the sintered Ti PTLs and anode catalyst layers are depicted in **Figure 2a and b** for the PTE and CCM, respectively. The representative catalyst volume renderings are consistent with our observation that the CCM configuration had a more uniform catalyst distribution, but still portrays two extremes: areas with catalyst clusters and large areas without catalyst. Furthermore, it seems the IrO_x electrocatalyst within the studied

resolution ($\sim 1 \mu\text{m}$) has poor in-plane connectivity for both configurations. CCM cross-section SEMs are shown in **Figure S1**, where layer morphology is shown too.

Ionic conductivity is essential to remove protons away from the reaction sites. In the case of the PTE MEA, some active sites are buried within the PTL. Adding ionomer to the catalyst ink can facilitate proton conduction away from the active site and to the PEM. On the other hand, electron conductivity is not a concern for the PTE configuration because the electrocatalyst is deposited directly onto a conductive titanium substrate. For the CCM, however, electrocatalyst is deposited onto the membrane and in some locations is not in direct contact with the Ti PTL. As such, in-plane electric conductivity is essential to remove electrons from the active sites and therefore poor in-plane conductivity can be performance-limiting. These effects are studied in more detail in Section 3.5.

The polarization curves for the PTE and CCM are plotted in **Figure 2c**. The polarization curve reproducibility study is shown in **Figure S2**. The CCM electrolyzer cell reaches higher current densities compared to the PTE cell for the same iR -corrected potentials. As current density increases, the difference between the two polarization curves increases. For example, at 800 mA/cm^2 the potential difference is more than 200 mV. The dissimilarity in polarization curves can be explained by the differences in ionic and electronic conductivity between the two MEAs which will be discussed in more detail in Section 3.5.

Nano-CT tomography scans allow further elucidation of the CCM catalyst distribution (the more uniform, and better performing

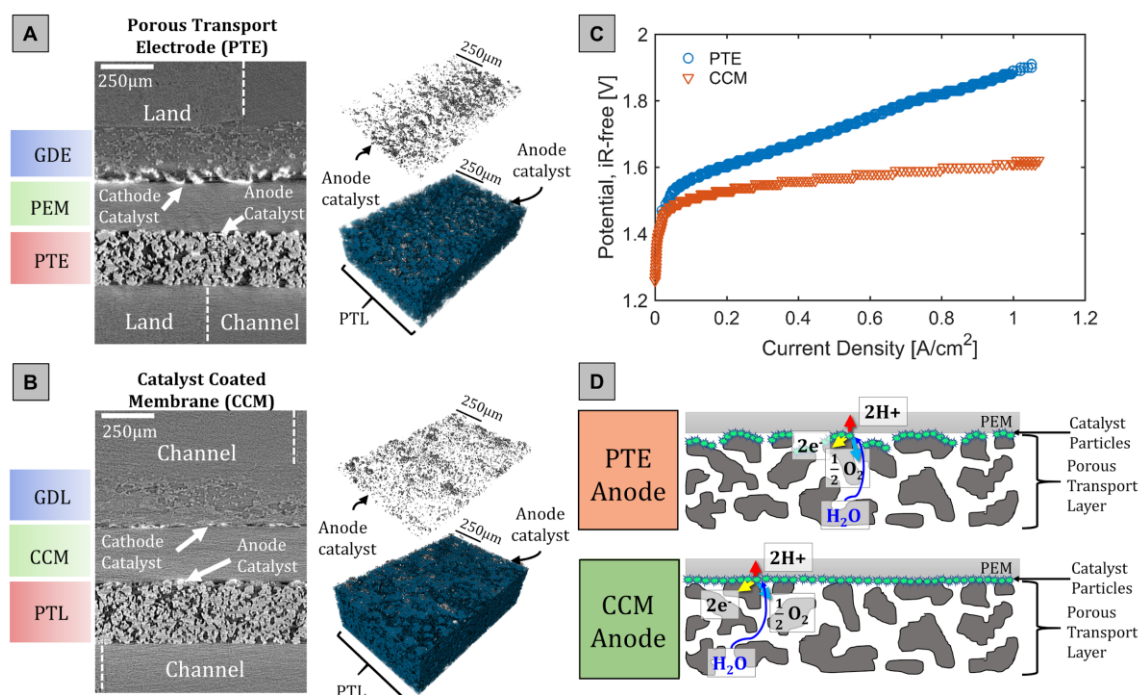


Figure 2. (a) Labeled tomographic cross section of the PTE MEA sample with the catalyst deposited on the electrodes (gas diffusion electrode (GDE) on the cathode and the porous transport electrode (PTE) on the anode). The anode catalyst layer (above, silver) was volume rendered separate from, and in combination with, the sintered titanium PTL (below, blue). Liquid water contacts the PTL from the channels on the anode side. (b) A labeled tomographic cross section of the CCM MEA sample with the catalyst layers deposited on the PEM. A volume rendering of the anode catalyst layer (above, silver) is depicted separate from, and interacting with, the sintered titanium PTL (below, blue). (c) The polarization curves for the PTE and the CCM MEA samples acquired just prior to the first operando scans. For the PTE electrolyzer cell the flow rate was 0.8 mL/min and the cell operated at 50°C . For the CCM cell the flow rate was 1 mL/min and the cell operated at 50°C . (d) A schematic of the anode side of the PEM electrolyzer for the two configurations each demonstrating the product separation transport for the electrons, protons and evolved oxygen gas through the solid titanium, PEM, and PTL pores, respectively.

of the two samples) at a smaller resolution of ~ 30 nm. The results of this are in **Figure 3**. **Figure 3a** shows the in-plane distance between two electrocatalyst clusters of (~ 7 μm) and **Figure 3b** is a volume rendering of this nano-CT scan supporting the non-uniformity

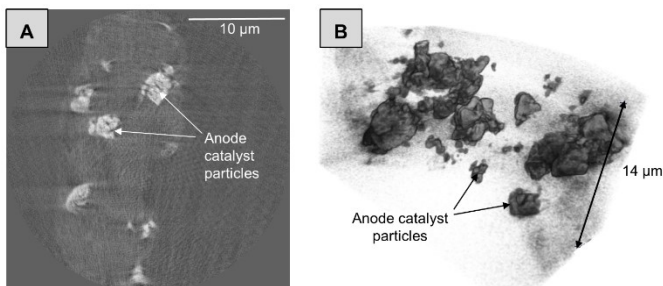


Figure 3. (a) Tomographic cross section from the NSLSII nano-CT experiments and (b) a volume rendering of the CCM anode catalyst layer showing the in-plane isolation of catalyst particles.

translating into three-dimensions. We observe significant agglomeration of IrO_x particles, and it is not clear, even with this high-resolution image, whether the nanoparticles present in the ionomer form an electrically percolating path between agglomerates.

Porous Transport Layer Morphologies

Due to the anode side of electrolyzers reaching corrosive potential levels for carbon paper, titanium is the preferred selection for the PTL material^{14–16}. Two different PTL morphologies were studied in CCM electrolyzer MEAs. **Figure 4** shows the tomographic cross sections for the sintered titanium (**Figure 4a**) and titanium fiber (**Figure 4b**) samples.

As can be seen in **Figure 4c**, the titanium fiber PTL cell outperformed the sintered titanium system at higher current densities. At $1 \text{ A}/\text{cm}^2$ Ti fiber PTE shows 45 mV improvement in cell potential. The polarization curve reproducibility study is shown in **Figure S2b**, where about 45 mV difference is preserved across different cell builds. Morphological analysis was conducted to understand the performance enhancement for the cell with Ti fiber. The three-dimensional renderings in **Figure 4a and b** show the catalyst distributions and the PTL morphologies for sintered titanium and titanium fiber PTLs, respectively. Each CCM has $2.2 \text{ mg}/\text{cm}^2$ anode catalyst loading, and as expected, the catalyst distributions look similar in the isolated catalyst volume renderings. The PTLs exhibit relative morphological uniformity across the thickness of the layer in contrast with fuel cell GDLs which often incorporate a microporous layer at the catalyst interface^{33–35}.

Tortuosity factor is a unitless value that represents how torturous, or convoluted, the pathways are within a porous network. To calculate the tortuosity factor we used the MatLab application TauFactor¹. TauFactor allows analysis in the thru-plane (defined here as the direction from the channels to the catalyst particles) and two in-plane (defined here as the two perpendicular directions parallel to catalyst particles). Since the porous network of both PTLs is not uniform, we analyzed all three directions and averaged the in-plane results. Both the void (pore) and solid (titanium) phases are important for reactant and product transport during the anode

electrochemical half reaction (**Eqn. 2**). The void network allows feed water transport to the catalyst particles and the evolved oxygen to diffuse and exit through the channels. Electrons freed during the reaction transport via the conductive titanium network to the BPPs.

Porosity and pore size distribution (PSD) are two PTL properties that provide additional context to tortuosity factor results. **Figure 5** shows the results of tortuosity factor, porosity, and PSD for the sintered titanium and titanium fiber PTLs.

Figure 5a and b report higher average tortuosity factor values for the void phase over the solid phase in both samples. This means the void pathways are more tortuous than the solid pathways which can be explained by the sample to have more solid phase rather than void. (**Figure 5f**). Sintered titanium has the highest void tortuosity factor of 3.9, compared to the Ti fiber PTL tortuosity factor of 3.3. This result is consistent with the average porosity of the two samples, with the lower average (0.36 void fraction) for sintered Ti.

The void phase for the two cases demonstrates anisotropic behavior with respect to tortuosity factor as the PTLs' in-plane values differ greatly from the thru-plane. Sintered Ti and Ti fiber had similar thru-plane tortuosity factors of 2.2 and 2.3, respectively. As stated

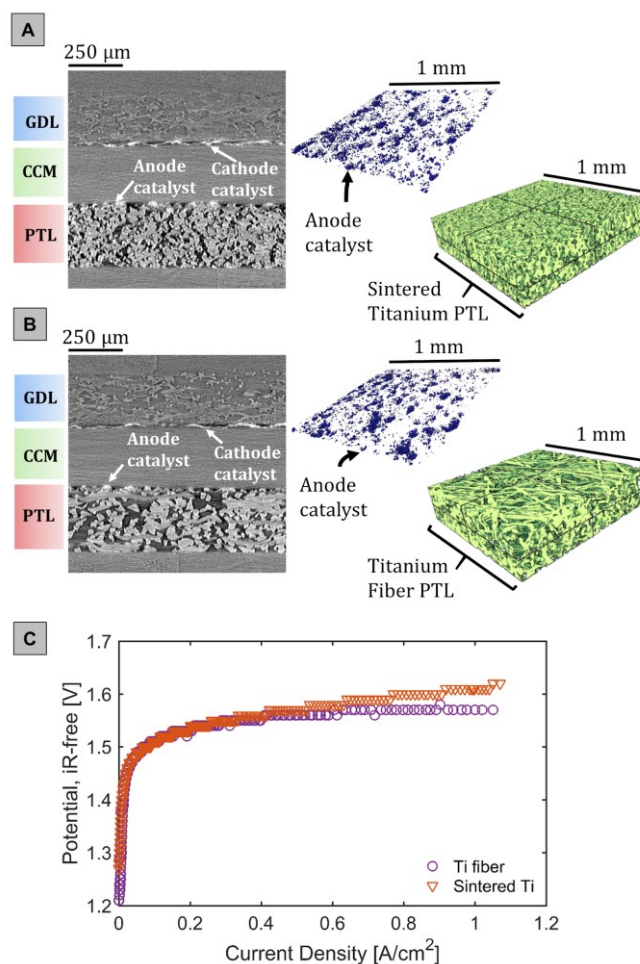


Figure 4. Titanium porous transport layer morphology and performance for the CCM electrolyzer MEAs. Tomographic cross sections and volume renderings of the anode catalyst distributions (above, blue) and PTL morphology (below, green) for (a) sintered titanium, with the cell operating at 50°C with an inlet water flow rate of $1 \text{ mL}/\text{min}$, (b) titanium fiber with the cell maintained at 50°C and a water flow rate of $1 \text{ mL}/\text{min}$. (c) Polarization curves for both of the PTL electrolyzer cells in which the dashed line represents titanium fiber and the solid line represents sintered titanium. Electrochemical tests were conducted at the beamline.

before, the difference between tortuosity in-plane factors for the two PTLs is mainly due to sintered Ti having lower volume fraction, but it is worth noting that the mechanism of laser sintering perhaps introduces directionality. For the fiber PTL, in-plane tortuosity is higher than thru-plane, which can be seen in the volume rendering (Figure 3b) as a higher quantity of void pathways are observable in the thru-plane direction compared to the in-plane direction. This result is in contrast with GDLs that are used in a fuel cell, which demonstrate the reverse tortuosity factor trend³³ where preferential fiber alignment allows a less restricted flow in-plane than in the thru-plane direction (i.e. a higher thru-plane tortuosity factor). The major differences between the Ti fiber PTLs and fuel cell carbon GDLs are the fabrication techniques and the porosity (the GDL porosity is often more than twice of that of the Ti fiber³⁶⁻³⁸). Here we do not observe strong preferential fiber orientation in-plane (Figure 4b). We also report representative, area-averaged stream-lines from the TauFactor simulations in SM, Figure S5, to show the path line of flow through the void fractions of both PTLs. Figure S5a and c support the similar tortuosity factors reported for both samples, but in-plane sintered Ti has a more uniform flux density (Figure S5b) than the flux density of titanium fiber (Figure S5d). This is consistent with the thru-plane and in-plane porosities for the two materials shown in SM, Figure 5a and b, respectively. Ti fiber in-plane porosity is consistently higher than sintered Ti with notable periodic exceptions (e.g. at ~0.3 mm and ~0.9 mm in Figure S6b), which is consistent with areas of higher flux depicted in the representative projection in

Figure S5d. Similarly, the sintered Ti has a uniform porosity across the in-plane width (Figure S6b) and a uniform flux density (Figure S5b).

The PTLs' PSD is expressed as a probability density function (PDF) histogram for the pore radii. Figure 5c and d show representative pore-size distributions for the sintered and fiber PTLs, respectively, and Figure 5e reports the mean pore radius which was the average of three analyzed volumes each. The Ti fiber PTL has larger average void radius size of 7.7 μm compared to sintered PTL of 5.4 μm , providing a less tortuous network for water and gas to transport through. Visual observations of the Ti fiber PTL volume rendering (Figure 4b) depicts pore openings in the thru-plane direction

to be larger than the 7.7 μm average. The smaller result is attributed to the BoneJ image analysis method. BoneJ computes the maximum spherical volume in the void phase before encountering a solid barrier. The resulting sphere diameter is exported as the local pore diameter. Thus, the fitted sphere method accounts for the shallower of the local in-plane and thru-plane directions. It should also be mentioned that the error bars included in Figure 5e represent one standard deviation calculated from three different sample results per PTL morphology. In both cases the error bar length is less than the pixel resolution so the actual error may be different. Porosity was calculated using segmented tomographic PTL volumes and it was found that Ti fiber had a higher porosity (44%) than sintered Ti (36%) (Figure 5f). An *ex-situ* PTL porosity characterization by weight resulted in porosities of 44% and 36%, for Ti Fiber and sintered Ti PTLs respectively, which is consistent with our image analysis technique.

Overall, higher porosity and larger pore-sizes are desirable when designing a PTL as they enable faster water and oxygen transport. Furthermore, higher porosity will result in lower void tortuosity, which seems to be one of the critical morphological factors. Fiber PTL did show a slightly higher current densities for the same applied iR-corrected potential, which can be attributed to its higher porosity, larger void sizes and lower void tortuosity, with overall low tortuosity values for the solid phase. This difference might become more pronounced at larger current densities, where mass-transport becomes increasingly significant.

Interfacial Analysis

Using tomography data for the two electrolyzer comparisons (PTE vs. CCM and sintered titanium PTL vs. titanium fiber PTL), we were able to quantify the interfacial connectivity of the catalyst and bordering phases. For the PTE we assumed that the catalyst was in direct contact with the PTL because the ink (catalyst particles and

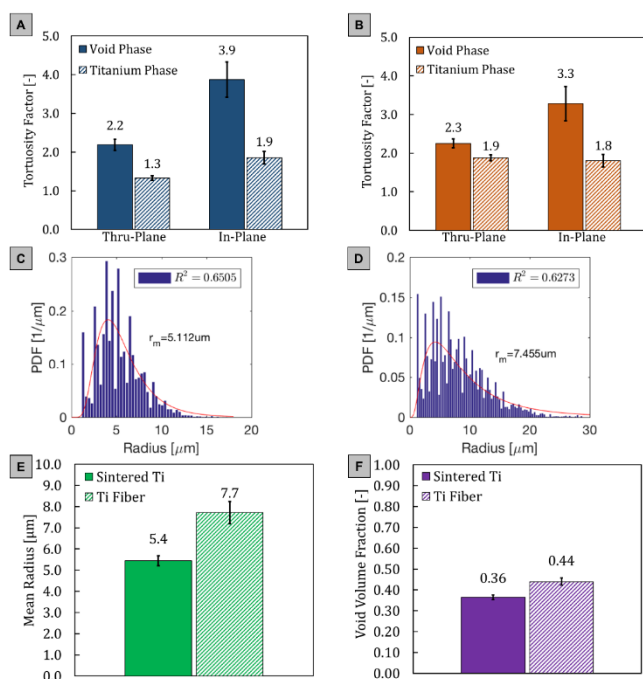


Figure 5. Tortuosity and pore size distribution results for the three different titanium PTL morphologies. Tortuosity factor was analyzed using the TauFactor¹ application for the solid (titanium) and void (pore) phases in the thru-plane and in-plane directions. For both metrics the analyzed samples were 1 mm² in the thru-plane perpendicular area. Results shown are for a minimum of three samples per PTL morphology. Average tortuosity factor results for (a) sintered titanium, and (b) titanium fiber PTLs. Representative void pore radius power density functions (PDF) are depicted graphically for (c) sintered titanium, (d) titanium fiber PTLs. The mean pore radius of the two PTL morphologies are graphically represented in (e) and porosities of the two samples are shown in (f) by void volume fraction.

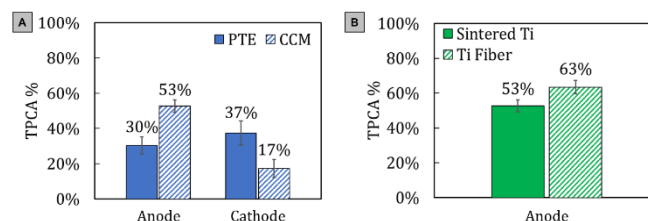


Figure 6. The results of the triple phase contact area (TPCA) at the catalyst interfaces for (a) the anode and cathode side of a PTE and CCM electrolyzer configurations and (b) the anode TPCA% for the two porous transport layer morphologies (sintered titanium and titanium fiber) in CCM MEAs.

ionomer) is directly deposited onto the titanium PTL. Similarly, we

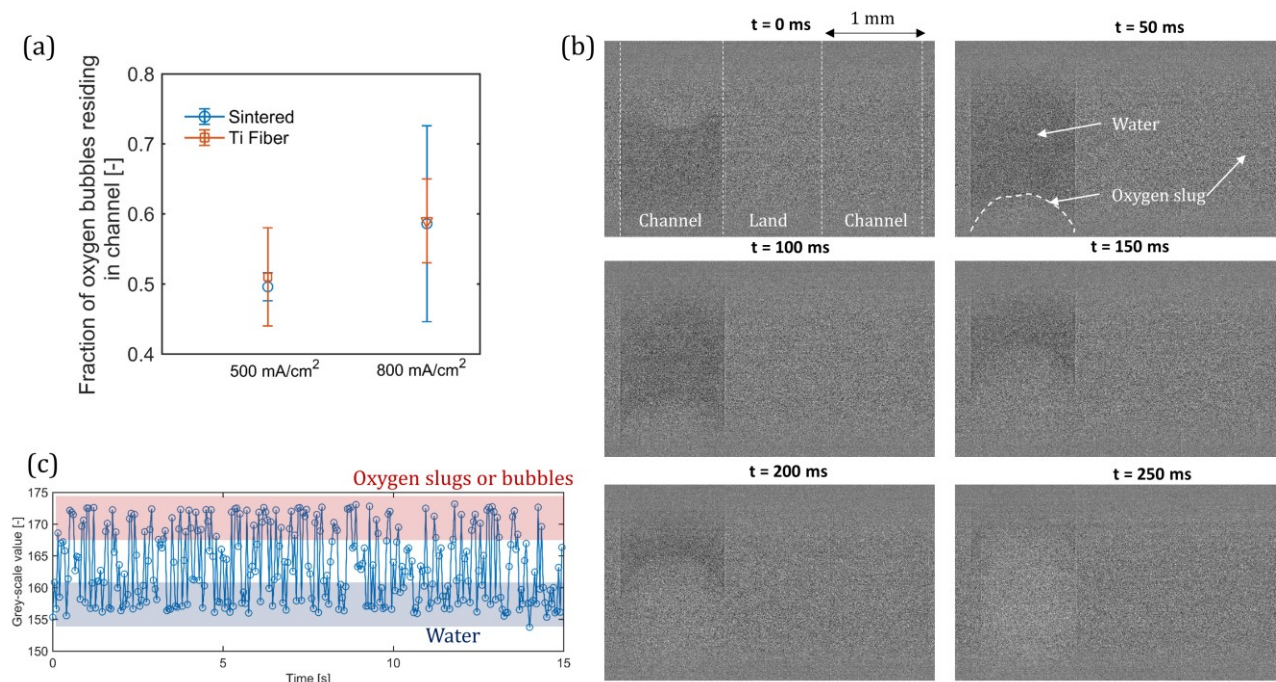


Figure 7. (a) Fraction of oxygen bubbles or slugs in the channel for two current densities and various PTL configurations. Gas slugs are when the gas is occupying the entire channel width. (b) Example of in-plane radiographs collected for 50°C, 500 mA/cm² and 50 ms exposure time. (c) An example of grey-scale values in a channel as a function of time for radiographs recorded over the period of 15 seconds (300 images).

assumed the catalyst particles and surrounding ionomer were in contact with the membrane for the CCM configuration, as the ink was directly deposited onto the membrane. **Figure 6** shows our results for TPCA ratio calculated using **Eqn. 4** and defined as the interfacial ratio of areas where transport layer, catalyst, and PEM are all in physical contact.

Figure 6a shows the anode side of the electrolyzer, where the OER occurs (**Eq. 2**); the CCM has a higher interfacial contact of 53% compared to the PTE of 30%. This is consistent with the electrolyzer performance shown by polarization curves in **Figure 2c** as the micro-CT CCM cell achieves superior performance with respect to the micro-CT PTE cell despite having lower catalyst loadings on both the anode and cathode. On the cathode side, the PTE had a higher catalyst connectivity at the interface. The PTE cathode had a higher catalyst loading than the cathode side of the CCM which explains the higher interfacial contact area for the PTE configuration. This did not notably affect performance because the OER on the anode side (**Eq. 2**) is the limiting half reaction for water electrolysis.

Figure 6b compares the interfacial contact area between two different PTL titanium morphologies. As shown in **Figure 4f**, sintered titanium has a higher solid fraction than titanium fiber. Even so, the titanium fiber TPCA exceeded the catalyst connectivity of the sintered titanium in a CCM system by 10 % (63 % for Ti fiber and 53 % for sintered Ti). Both CCMs had the same anode catalyst loading. From SM, **Figure S6a** we observe the thru-plane porosity as consistent for both PTLs. Therefore, we believe the slight difference in TPCA in favor of the Ti fiber is due to the PEM being more conformal with the fiber PTL at the interface. The polarization curves in **Figure 4c** are consistent with this contact result as the titanium fiber PTL electrolyzer performed slightly better than the sintered

titanium in our micro-CT electrolyzer cell.

Radiography

From radiography we calculated fraction of oxygen bubble residence in the channel, where '0' indicates the channel is filled by water and '1' when the channel is filled by oxygen (**Figure 7**). From **Figure 7a**, for 500 mA/cm² and 800 mA/cm² both sintered Ti and Ti fiber showed similar fractions of oxygen in the channel ~0.5 and 0.6, respectively. As already mentioned above, the polarization curves in this lower current density regime were also similar for these two PTLs. Therefore, the selection of using sintered Ti or Ti fiber as the PTL when operating below 1 A/cm² is not as critical, as mass-transport is not the dominant cause of overpotentials.

Modeling

Using the simulation model, polarization curves were simulated for CCM and PTE configurations. **Figure 8a** shows the simulated polarization curves for both configurations.

Quantitatively, the model shows performance similar to the experimental results in **Figure 2c**, with the CCM performing better than the PTE configuration in both cases. While analyzing the electronic potential profile in CCM configuration, no significant effect was found due to the discrete solid-void configuration as long as an electrically percolating network of particles exists. The continuum model does not capture the discrete nature of connecting particles, and if the network is not electrically percolating the electric connectivity can be limiting. In the anode catalyst layer there are no electrically conductive supports to enhance electric conductivity.

In the PTE configuration, connectivity of the catalyst layer to the

membrane plays a critical role as shown in **Figure 8b**. The points of contact between the catalyst layer and membrane were simulated given the sintered Ti PTL morphology, as shown by **Figure S7**. Since

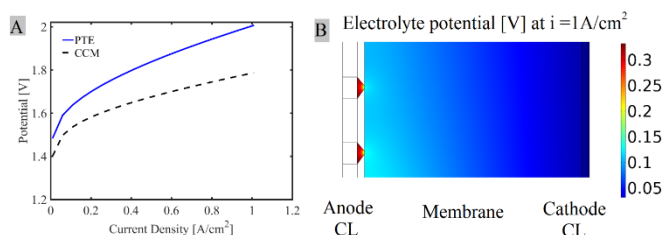


Figure 8. Cell performance results from simulation model. (a) Pol-curves for PTE and CCM, (b) PTE electrolyte potential profile at 1 A/cm².

in the PTE configuration catalyst ink conforms to the Ti PTL the contact points between the catalyst layer and membrane can be simulated with the PTL geometry. Significant ionic potential loss occurs at the constriction points where catalyst layer meets membrane. Bottlenecks are formed in proton conduction pathways due to low connectivity between catalyst layer and the membrane, due to the rough interface, resulting in high flux and therefore significant potential gradients.

Conclusions

In this study we use X-ray CT and radiography to visualize morphology and oxygen transport in PEM electrolyzers. We use electrochemical polarization curves to quantify the micro-CT electrolyzer cell performance. First, we compare performance of two different electrolyzer MEA configurations, CCM and PTE. We correlate the polarization curves to interface morphology observed with X-ray CT. At 1 A/cm², the micro-CT CCM electrolyzer showed 200 mV improvement in potential primarily due to better contact between the electrocatalyst, membrane, and PTL. From the nano-CT imaging we discovered non-homogeneous distribution of IrO_x electrocatalyst and from the images it is also not clear whether the larger IrO_x agglomerates are electrically connected via a percolating conductive network of nanoparticles. This results in poor in-plane connectivity from the non-uniform and disconnected catalyst dispersion on the anode side of the electrolyzer.

Then, we compared the polarization behavior and morphology of cells with CCMs but two different titanium PTLs. One was made with sintered Ti and the other with Ti fiber. The Ti fiber PTL showed higher porosity, larger pore sizes and lower tortuosities, both in-plane and thru-plane, translating into slightly lower cell potentials. At 1 A/cm² the Ti fiber cell had potential lower by 45 mV compared to the sintered Ti cell. In our radiography study, oxygen residence in the channels showed similar fractions for both types of PTLs, indicating minor differences in oxygen transport properties of these PTLs. Furthermore, the CCM in contact with the Ti fiber PTL showed higher contact area, which might be due to better conformity of fibers vs. the solid phase of the sintered Ti PTL.

The modeling study shows that the primary reason for performance loss in the PTE configuration is due to low ionic connectivity of catalyst layer with membrane. This causes bottlenecks in proton transport and results in high potential losses in

anode.

Conflicts of interest

There is no conflict to declare

Acknowledgements

All of the authors would like to acknowledge funding from the HydroGEN Advanced Water Splitting Materials Consortium, established as part of the Energy Materials Network under the U.S. Department of Energy, Office of Energy Efficiency and Renewable Energy, Fuel Cell Technologies Office and program managers David Peterson and Katie Randolph. This work was supported by DOE EERE award number EE0008081. This research used beamline 2-BM-A of the Advanced Photon Source, a U.S. Department of Energy (DOE) Office of Science User Facility operated for the DOE Office of Science by Argonne National Laboratory under Contract No. DE-AC02-06CH11357. This research used beamline 8.3.2 of the Advanced Light Source, which is a DOE Office of Science User Facility under contract no. DE-AC02-05CH11231. This research used beamline 18-ID of the National Synchrotron Light Source II, a U.S. Department of Energy (DOE) Office of Science User Facility operated for the DOE Office of Science by Brookhaven National Laboratory under Contract No. DE-SC0012704. Authors would like to thank Dr. Jie Zhou at LBNL for help with electrolyzer model and Ying Huang from UCI for help with nano-CT analysis and visualization. We thank Dr. Dinesh Sabarirajan and Mr. Stanley Normile with the initial electrolyzer set-up development and testing. We thank Dr. Andrea Perego for SEM images of the CCM.

References

1. S. J. Cooper, A. Bertej, P. R. Shearing, J. A. Kilner and N. P. Brandon, *SoftwareX*, 2016, **5**, 203-210.
2. K. Mazloomi and C. Gomes, *Renewable and Sustainable Energy Reviews*, 2012, **16**, 3024-3033.
3. P. Nejat, F. Jomehzadeh, M. M. Taheri, M. Gohari and M. Z. Abd. Majid, *Renewable and Sustainable Energy Reviews*, 2015, **43**, 843-862.
4. A. Lewandowska-Bernat and U. Desideri, *Applied Energy*, 2018, **228**, 57-67.
5. U. Babic, M. Suermann, F. N. Büchi, L. Gubler and T. J. Schmidt, *Journal of The Electrochemical Society*, 2017, **164**, F387-F399.
6. T. Schuler, R. De Bruycker, T. J. Schmidt and F. N. Büchi, *Journal of The Electrochemical Society*, 2019, **166**, F270-F281.
7. A. Züttel, A. Remhof, A. Borgschulte and O. Friedrichs, *Philosophical Transactions of the Royal Society A: Mathematical, Physical and Engineering Sciences*, 2010, **368**, 3329-3342.
8. M. M. Rashid, M. K. Al Mesfer, H. Naseem and M. Danish, *Int. J. Eng. Adv. Technol.*, 2015, **4**, 2249-8958.
9. B. Pivovar, N. Rustagi and S. Satyapal, *The Electrochemical Society Interface*, 2018, **27**, 47-52.
10. A. Buttler and H. Spliethoff, *Renewable and Sustainable Energy Reviews*, 2018, **82**, 2440-2454.

11. B. Han, J. Mo, Z. Kang and F.-Y. Zhang, *Electrochimica Acta*, 2016, **188**, 317-326.
12. P. Lettenmeier, S. Kolb, N. Sata, A. Fallisch, L. Zielke, S. Thiele, A. S. Gago and K. A. Friedrich, *Energy & Environmental Science*, 2017, **10**, 2521-2533.
13. K. E. Ayers, E. B. Anderson, C. Capuano, B. Carter, L. Dalton, G. Hanlon, J. Manco and M. Niedzwiecki, *Ecs Transactions*, 2010, **33**, 3-15.
14. S. A. Grigoriev, P. Millet, S. A. Volobuev and V. N. Fateev, *International Journal of Hydrogen Energy*, 2009, **34**, 4968-4973.
15. P. Lettenmeier, S. Kolb, F. Burggraf, A. S. Gago and K. A. Friedrich, *Journal of Power Sources*, 2016, **311**, 153-158.
16. J. Seweryn, J. Biesdorf, T. J. Schmidt and P. Boillat, *Journal of The Electrochemical Society*, 2016, **163**, F3009-F3011.
17. L. T. Soo, K. S. Loh, A. B. Mohamad, W. R. W. Daud and W. Y. Wong, *Applied Catalysis A: General*, 2015, **497**, 198-210.
18. L. Du, Y. Shao, J. Sun, G. Yin, J. Liu and Y. Wang, *Nano Energy*, 2016, **29**, 314-322.
19. S. Siracusano, V. Baglio, A. Di Blasi, N. Briguglio, A. Stassi, R. Ornelas, E. Trifoni, V. Antonucci and A. Arico, *International journal of hydrogen energy*, 2010, **35**, 5558-5568.
20. S. Grigoriev, V. Porembsky and V. Fateev, *International Journal of Hydrogen Energy*, 2006, **31**, 171-175.
21. Z. Kang, G. Yang, J. Mo, S. Yu, D. A. Cullen, S. T. Retterer, T. J. Toops, M. P. Brady, G. Bender, B. S. Pivovar, J.B. Green Jr, F.-Y. Zhang, *International Journal of Hydrogen Energy*, 2018, **43**, 14618-14628.
22. L. Zielke, A. Fallisch, N. Paust, R. Zengerle and S. Thiele, *RSC Advances*, 2014, **4**, 58888-58894.
23. E. Leonard, A. D. Shum, S. Normile, D. C. Sabarirajan, D. G. Yared, X. Xiao and I. V. Zenyuk, *Electrochimica Acta*, 2018, **276**, 424-433.
24. M. Nourani, B. I. Zackin, D. C. Sabarirajan, R. Taspinar, K. Artyushkova, F. Liu, I. V. Zenyuk and E. Agar, *Journal of The Electrochemical Society*, 2019, **166**, A353-A363.
25. F. De Carlo, D. Gursoy, F. Marone, M. Rivers, D. Y. Parkinson, F. Khan, N. Schwarz, D. J. Vine, S. Vogt, S.-C. Gleber, S. Narayanan, M. Newville, T. Lanzirrotti, Y. Sun, Y. P. Hong and C. Jacobsen, *Journal of Synchrotron Radiation*, 2014, **21**, 1224-1230.
26. B. A. Dowd, G. H. Campbell, R. B. Marr, V. V. Nagarkar, S. V. Tipnis, L. Axe and D. P. Siddons, *Developments in synchrotron x-ray computed microtomography at the National Synchrotron Light Source*, SPIE, 1999.
27. D. M. Pelt, D. Gursoy, W. J. Palenstijn, J. Sijbers, F. De Carlo and K. J. Batenburg, *Journal of Synchrotron Radiation*, 2016, **23**, 842-849.
28. D. Gursoy, F. De Carlo, X. Xiao and C. Jacobsen, *Journal of Synchrotron Radiation*, 2014, **21**, 1188-1193.
29. A. D. Shum, D. Y. Parkinson, X. Xiao, A. Z. Weber, O. S. Burheim and I. V. Zenyuk, *Electrochimica Acta*, 2017, **256**, 279-290.
30. A. Serov, A. D. Shum, X. Xiao, V. De Andrade, K. Artyushkova, I. V. Zenyuk and P. Atanassov, *Applied Catalysis B: Environmental*, 2018, **237**, 1139-1147.
31. C. A. Schneider, W. S. Rasband and K. W. Eliceiri, *Nature Methods*, 2012, **9**, 671.
32. M. Doube, M. M. Kłosowski, I. Arganda-Carreras, F. P. Cordelières, R. P. Dougherty, J. S. Jackson, B. Schmid, J. R. Hutchinson and S. J. Shefelbine, *Bone*, 2010, **47**, 1076-1079.
33. I. V. Zenyuk, P. K. Das and A. Z. Weber, *Journal of The Electrochemical Society*, 2016, **163**, F691-F703.
34. S. J. Botelho and A. Bazylak, *Journal of Power Sources*, 2015, **280**, 173-181.
35. S. Park, J.-W. Lee and B. N. Popov, *Journal of Power Sources*, 2006, **163**, 357-363.
36. I. V. Zenyuk, D. Y. Parkinson, G. Hwang and A. Z. Weber, *Electrochemistry Communications*, 2015, **53**, 24-28.
37. X. L. Wang, H. M. Zhang, J. L. Zhang, H. F. Xu, Z. Q. Tian, J. Chen, H. X. Zhong, Y. M. Liang and B. L. Yi, *Electrochimica Acta*, 2006, **51**, 4909-4915.
38. S. Park and B. N. Popov, *Fuel*, 2011, **90**, 436-440.